Journal of Applied Fluid Mechanics, Vol. 17, No. 10, pp. 2154-2168, 2024.
Available online at www.jafmonline.net, ISSN 1735-3572, EISSN 1735-3645.
https://doi.org/10.47176/jafm.17.10.2622

Coupled Effects of Hub Diameter Ratio and Blade Angle on the Performance of Spiral Axial Flow Gas Liquid Multiphase Pump

W. Han[1,2], S. Q. Yang[1], R. N. Li[1,3†], Y. P. Tian[4], and T. Yang[1]

[1] *School of Energy and Power Engineering, Lanzhou University of Technology, Lanzhou, Gansu 730050, China*
[2] *Key Laboratory of Advanced Pumps Valves and Fluid Control System of the Ministry of Education, Lanzhou University of Technology, Lanzhou, Gansu 730050, China*
[3] *Key Laboratory of Fluid machinery and Systems, Lanzhou, Gansu 730050, China*
[4] *Gansu water resources and Hydropower Survey and Design Research Institute Co., Ltd, Lanzhou, Gansu, 730000, China*

†Corresponding Author Email: 231080704004@lut.edu.cn

ABSTRACT

In pursuit of enhancing the conveying performance of the spiral axial flow gas-liquid multiphase pump, a comprehensive exploration is conducted to unravel the underlying influence mechanism of impeller structural parameters on gas-liquid separation. This study employs the Box-Behnken design, constructing a sample space that encompasses crucial factors such as impeller hub parameters and blade inclination angle, utilizing Computational Fluid Dynamics software to perform numerical simulations of various models within the sample space. Researching the influence of impeller hub diameter ratio and blade inclination angle on the internal flow of a multiphase pump, aiming to determine high-performance parameters under high gas content conditions with the coupled effects of impeller hub diameter ratio and blade inclination angle. The results indicate that the performance improvement becomes more pronounced when the blade inclination angle (γ) is greater than 2°. For hub structure parameters, the relative size of hub inlet coefficient (k_{d1}) and hub middle section coefficient (k_{d2}) is measured using the diameter ratio (kr), where kr ranges from 0.94 to 1.02. After optimization, the impeller hub parameters are k_{d1} = 0.77, k_{d2} = 0.76, kr = 1.013, γ = 6.95. In comparison with the original model, when the Inlet Gas Volume Fraction is 60%, the gas phase aggregation (λ) at 0.1Span is reduced by 4.5%, the energy dissipation (σ) is decreased by 5.3%, and the efficiency and head coefficient are increased by 2.331% and 0.05, respectively. Therefore, this study has vital theoretical and technical significance for improving the reliability, stability and efficiency of deepwater oil and gas transportation.

Article History

Received January 24, 2024
Revised April 12, 2024
Accepted May 3, 2024
Available online July 31, 2024

Keywords:

Spiral axial flow gas-liquid multiphase pump
Hub diameter ratio
Blade inclination angle
Gas phase aggregation
Energy dissipation

1. INTRODUCTION

The demand for primary energy is increasing with the continuous development of the industrial landscape, particularly oil and natural gas, has surged. Given the steady growth rate of global crude oil demand and the substantial volume of production, it is anticipated that there will be no substantial decline in the extraction, consumption, or trading of crude oil in the foreseeable future. Nevertheless, existing onshore and shallow offshore oil and gas exploration and production activities are insufficient to meet the long-term development requirements. In recent years, there has been a notable increase in the share of proven deep-water oil and gas reserves, indicating a shifting trend toward the exploration and extraction of crude oil in remote deep-sea wells. Simultaneously, deep-sea extraction encounters intricate extraction conditions characterized by crude oil, often accompanied by sand, water, and natural gas. These challenges impose greater demands on the efficiency and stability of dynamic systems.

To address these challenges, a technological multiphase pump was developed and partially implemented. The technology has been successfully applied to deep water and many remote oil fields (Bratu, 1995; Saadawi, 2007). An exemplary solution in this domain is the multiphase pump developed by Sulzer (Gié et al., 1992; Falcimaigne et al., 2002), which satisfies the demands of high flow and mitigates the impact of sand on performance. This pump has garnered widespread adoption and has yielded favorable outcomes in various oil fields (Leporcher et al., 2001; Grimstad, 2004; Saadawi, 2008). However, in the process of transporting

NOMENCLATURE

ANN	Artificial Neural Networks	RANS	Reynolds-averaged Navier-Stokes
ANOVA	Analysis of Variance	R^2	coefficient of determination
BBD	Box-Behnken design	$S_{GVF\geq0.8}$	area of the grid where the gas content in the analysis domain is not less than 0.8
CCD	Central Composite design	$S_{k\geq10}$	are of the regional grid with turbulent kinetic energy not less than 10 m^2/s^2 in the analysis domain
CFD	Computational Fluid Dynamics	Span	blade height
D	impeller diameter	SST	Shear Stress Transfer
D_1	hub inlet diameter	u_2	impeller outlet circumference velocity
D_2	diameter of the middle segment	y_i	value contained in the data set
F_D	drag forces	$\bar{y}$	average value of the data set
F_P	pressure gradient	Z	number of impeller blades
f_i	predicted value of the response surface	z	distance of axial section from inlet
g	local acceleration of gravity	β_1	blade inlet placement angle
H	axial length	β_2	blade outlet placement angle
IGVF	Inlet Gas Volume Fraction	γ	blade inclination angle
k_{d1}	hub inlet coefficient	σ	energy dissipation
k_{d2}	hub middle section coefficient	λ	gas phase aggregation
kr	hub diameter ratio	η	efficiency
MRF	Multiple Reference Frame	ψ	head coefficient
NSGA	Non-dominated Sorting Genetic Algorithm	θ	hub half cone angle

gas-liquid mixed media in the operation of the pump, when the gas content at the entrance exceeds 30%, the difference in the density of the two phases will eventually cause the obvious boundary between the gas phase and the liquid phase medium, coupled with the effect of adverse pressure gradient, resulting in the gas phase stagnation at the back of the impeller and intermittent blockage of the flow channel. Ultimately, this instability in the internal flow field results in a decline in the pumping performance.

In gas-liquid two-phase flows, research on the intake conditions and bubble behavior in axial flow pumps has been conducted since the 1980s (Murakami & Minemura, 1983a, b). The movement of the bubble is affected by the pressure gradient force, the drag force between the gas and liquid phase and the inertia force generated by the liquid phase virtual mass (Murakami & Minemura, 1980). However, the movement behavior of the bubble inside the impeller is mainly determined by the balance between the pressure gradient (F_P) and the resistance (F_D) forces. The ratio of F_P to F_D increases with the increase of bubble diameter and impeller speed, but decreases with the increase of liquid flow. This balance ultimately determines whether the bubbles leave or remain in the impeller (Stel et al., 2019).

With an increase in the flow field gradient, the rate of performance degradation exhibits a linear relationship because the impact of the flow channel blockage on the performance degradation remains consistent regardless of the internal flow field characteristics (Suh et al., 2017). Variations in the drag and lift coefficients directly influence the liquid velocity and gas-phase distribution (Mohajerani et al., 2012). Furthermore, studies have uncovered the relationship between the interphase forces and the velocity difference between gas phase and the liquid phase, and the gas-phase volume fraction (Liu et al., 2018a). In the multiphase flow within the impeller, bubbles originate on the working face of the high-pressure side, gradually traverse towards the blade's midsection, and ultimately migrate to the suction surface of the low-pressure side. Periodic shedding occurs at the impeller exit. (Shi et al., 2019b).

The influence of the separation phenomenon on the internal flow of the fluid machinery has also been gradually revealed (Liu et al., 2023). Scholars have begun to explore the impact of impeller structure on the gas-liquid separation problem. They initially achieved this by altering the blade angles of the impeller and the blade angles of the diffuser. Following the modification of the multiphase pump, with adjustments made to the 10% of the inlet gas phase volume fraction, there was an increase in pressurization by 12.8 kPa, stabilizing the gas phase distribution in the flow field (Liu et al., 2018b). The influence of blade modification on the flow characteristics and pressure pulsation in the impeller channel is also revealed (Wu et al., 2021). By modifying the leading-edge radius, the boosting capability of the impeller can be enhanced, reducing the occurrence of secondary flow losses near the impeller outlet, suppressing gas accumulation near the hub side, and mitigating gas-liquid separation phenomena within the flow channel (Ma et al., 2020). In addition, by adding short blades, opening holes in the blades where bubbles gather and adopting T-shaped blades and other optimization measures, the gas-liquid mixing degree in the flow channel can be enhanced and the pressurization capacity of the impeller can be improved (Zhang et al., 2012). For the same hub thickness, reducing the thickness ratio coefficient, the operation performance of the pump can be improved and the gas accumulation degree in the pump can be reduced (Han et al., 2020).

Objective optimization techniques have been applied to optimize impeller design (Pei et al., 2019). This involves the integration of Artificial Neural Networks (ANN) with the Non-dominated Sorting Genetic Algorithm (NSGA-II) (Zhang et al., 2011). To

establish the sample space through an orthogonal design of the experimental methodology, utilizing the primary geometrical parameters that influence impeller performance as the optimization variables, a method for optimization of pump impellers is formulated. Response surface and numerical analyses also play important roles in the optimization of pumps (Kim et al., 2015). This research employs a combination of numerical simulations and experiments, with numerical simulation techniques emerging as crucial tools for studying fluid flows (Li et al., 2023a, b, c).

Current research on hub structure relies on hub ratio (Shi et al., 2019a), which can only describe the "straight-cone" hub structure and cannot account for the variability in hub curvature. The hub-diameter ratio significantly affected the rate of change in the flow area in the flow channel. Based on the principles of hydrodynamics, the variation in the flow channel area generates a variable acceleration within the channel. This acceleration acts on the fluid microclusters, propelling their movement toward the trailing edge of the blade grid. Moreover, existing studies on inclined blades (Ma et al., 2015) lack clarity regarding the enhancement of the internal flow field in mixed-transport pumps using inclined blade angles. In some cases, this may even lead to a reduction in the conveying performance of mixed-transport pumps. Building upon relevant research on hub structure and blade inclination, this study considers the blade inclination angle, hub inlet diameter, and middle section diameter as design factors. The head coefficient and efficiency were selected as the design variables to explore the coupled effects of the hub diameter ratio and blade inclination angle on the performance.

A polynomial-function response surface was generated to analyze the coupling effects. This study identified high-performance parameters for the coupling of hub diameter ratio and blade angle under conditions of high Inlet Gas Volume Fraction (IGVF). Through the optimization of impeller parameters, this study achieves the goal of improving gas-liquid separation in deep-sea oil and gas exploitation, while enhancing the conveying performance of mixed transport pumps. These findings provide crucial theoretical support and practical guidance for deep-sea oil and gas exploitation.

2. RESEARCH OBJECT

To further investigate the impact of the hub diameter ratio and blade inclination angle on gas-liquid separation, a spiral axial flow gas-liquid multiphase pump was selected as the focal point of this study. The pump is modeled using creo, which consists of four main parts, as shown in Fig. 1 The study was conducted with a designated flow rate of 100 m^3/h, a head of 30 m, and an operational speed of 4500 rpm. Table1 lists the key parameters of the impeller structure.

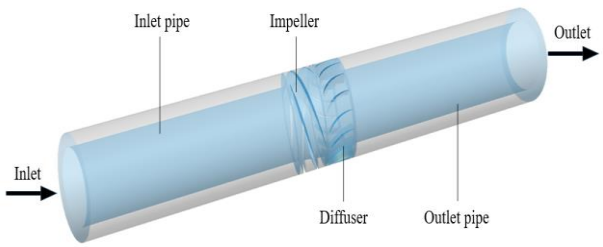

Fig. 1 Fluid domain model

Table 1 Impeller Structural Parameters

Symbol	Structural parameters	Parameter value
D_2	Impeller diameter (mm)	150
Z	Number of impeller blades	4
θ	Hub half cone Angle (°)	6
e	Axial length (mm)	55
β_1	Blade inlet placement Angle (°)	10
β_2	Blade outlet placement Angle(°)	14

3. NUMERICAL CALCULATION METHOD

The flow within the helical axial-flow gas-liquid mixed transport pump is characterized by viscous fluid, three-dimensional, incompressible turbulent flow. The governing equations consist of the continuity equation and the momentum conservation equation derived based Reynolds-averaged Navier-Stokes (RANS). Utilizing the finite volume method, convergence accuracy is set to 10^-5, and the variation in head is monitored to ensure the precision and reliability of the numerical simulation.

The turbulence model of numerical calculation is SST k-ω model. In contrast to other turbulence models, this model primarily accounts for the transmission of turbulent shear stress in adverse pressure gradients, thereby enabling the prediction of fluid separation points and regions under adverse pressure gradient conditions– The liquid separation within the flow channel is a critical factor that influences the performance of the multiphase pumps. Adopting the turbulence model facilitates a more precise calculation of the flow phenomena within the multiphase pump.

3.1 Grid Division

The four parts of the fluid domain grid are consistent with the four parts of the three-dimensional model. The entire domain was meshed using Fluent Meshing in Workbench software. The selected mesh generation technique is polyhedral meshing, which offers superior mesh quality and improved numerical stability. In addition, the use of a smaller boundary layer volume enables the capture of finer details near the flow field boundary. Compared to other mesh types, polyhedral meshes significantly reduce the number of required meshes while still meeting the computational requirements, thereby reducing both the computational time and the consumption of computational resources. The global grid is illustrated in Fig. 2, and Fig. 3 shows the impeller and boundary layers.

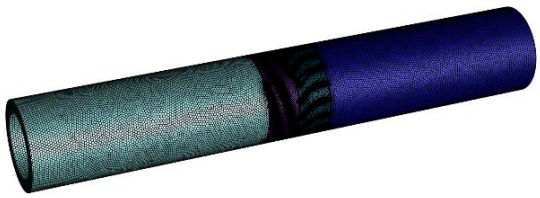

Fig. 2 Global grid of fluid domain

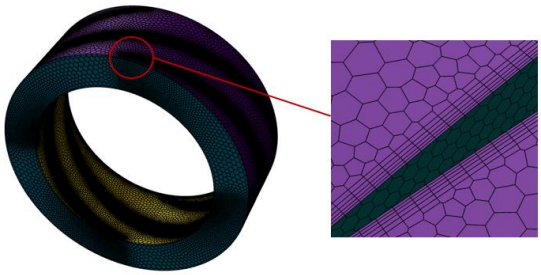

Fig. 3 Impeller grid and boundary layer

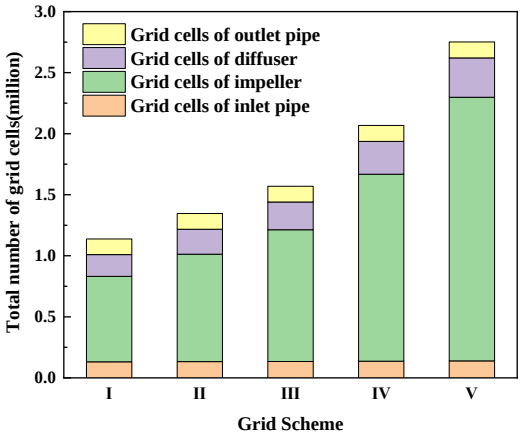

Fig. 4 Grid number of each scheme

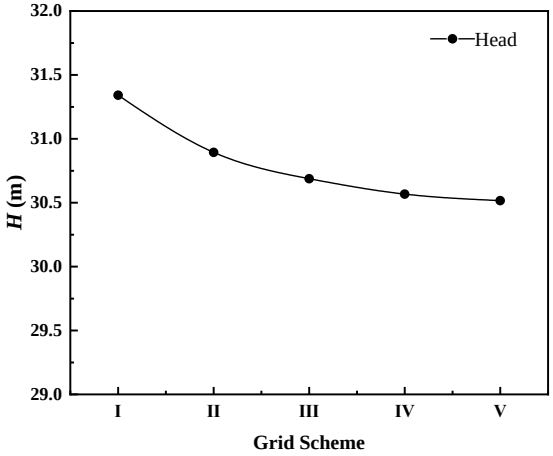

Fig. 5 Grid independence verification

Figure 4 presents the grid count for each scheme and Fig. 5 illustrates the variation in the head for each grid scheme. When the grid count exceeded 2 million, the head no longer exhibited a significant decrease with further grid refinement. Considering the balance between the computational efficiency and accuracy, scheme IV was ultimately chosen as the grid scheme for subsequent numerical simulations.

3.2 Boundary Conditions and Initial Conditions

In the numerical simulation of the multiphase pump water and air were selected as the flow media. In this study, water was considered as the primary phase, characterized by an incompressible nature and a density of 998.2 kg/m^3 at a standard temperature. The secondary phase consists of incompressible air with a density of 1.225 kg/m^3 at room temperature. The bubble diameter was set as 0.1 mm.

In numerical simulations, the establishment of appropriate initial conditions and boundary conditions holds significant importance. These conditions define the initial state of the problem and the constraints imposed on the system's boundaries, ensuring the accuracy and reliability of the simulation results. In this study, inlet boundary conditions are set to: velocity inlet; The outlet boundary condition is set to: pressure outlet. For steady-state conditions, the Multiple Reference Frame (MRF) is used, with rotating walls applied in the rotating domain, and non-slip walls used elsewhere. Conformal interfaces are implemented for mesh interfaces, facilitating data transfer across internal surfaces.

3.3 Experimental Verification

The experimental investigation primarily aimed at testing the performance of the system under flow conditions with an IGVF of 50. Figure 6 presents a comparison between the experimental data and the external characteristic curves obtained through the numerical simulation, indicating a general agreement between the numerical simulation and experimental findings. The numerical simulation does not account for friction losses owing to roughness or losses along the route. However, the error range of the head and efficiency remains within an acceptable range of 5–10%, confirming the accuracy and dependability of the numerical simulation. Figure 7 shows that:Performance test bench of gas-liquid two-phase flow pump.

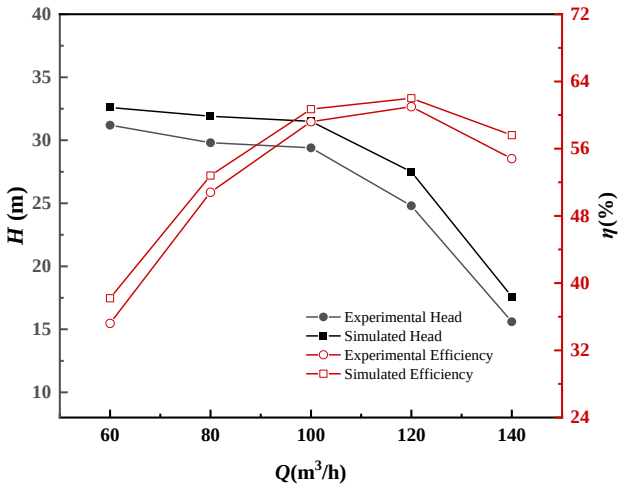

Fig. 6 Comparison between numerical simulation and experimental data of the original model

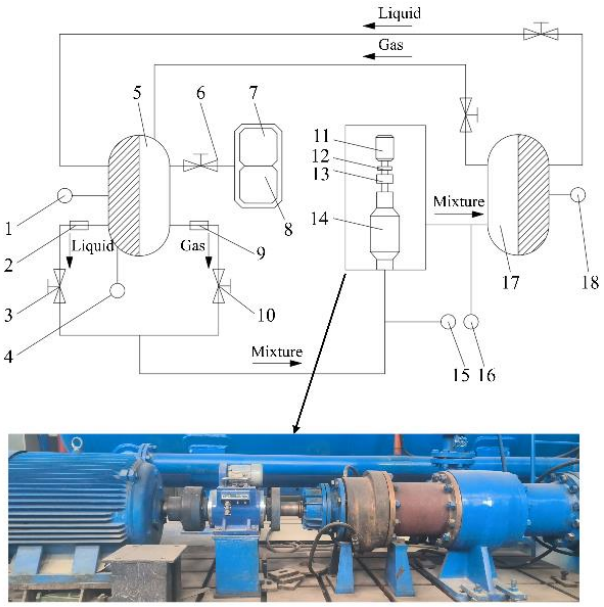

1,4,15,16, 18- Pressure gage; 2- Flow gauge; 3- Liquid inlet valve;5-Pressure tank; 6- Air valve; 7,8-Compressor; 9- Flow meter;10 Intake valve; 11 Motor; 12 Coupling; 13 Torque sensor; 14 Model pumps; 17 Medium pressure tank

Fig. 7 Performance test bench of gas-liquid two-phase flow pump

4. OPTIMIZATION BASED ON THE RESPONSE SURFACE METHOD

4.1 Response Surface Design

Response surface design commonly employs advanced methods, such as the Box-Behnken design (BBD) and Central Composite design (CCD). BBD is particularly well-suited for optimizing experiments involving two to five factors (Wang et al., 2013). To enhance the universality of the conclusions and obtain more definitive results, a dimensionless treatment was applied to both the diameter of the hub inlet and the middle section of the hub.

The dimensionless coefficient k_{d1} for the inlet section diameter of the impeller hub is defined as

$$k_{d1} = \frac{D_1}{D} \tag{1}$$

Here, D_1 represents the hub inlet diameter, D denotes the impeller diameter. The dimensionless coefficient k_{d2} for the middle section diameter of the wheel hub is defined as

$$k_{d2} = \frac{D_2}{D} \tag{2}$$

Here, D_2 represents the diameter of the middle segment. The relative sizes of the hub inlet and middle section diameters directly affected the acceleration of fluid microclusters in the impeller. Therefore, the dimensionless parameter kr was introduced to describe the relative sizes of D_1 and D_2, and the diameter ratio kr of the middle section was

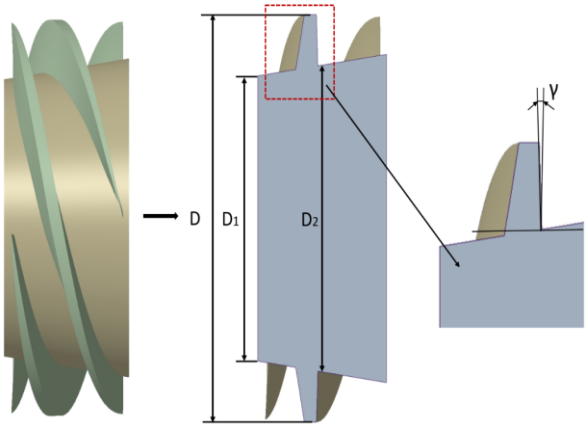

Fig. 8 Schematic diagram of parameters

$$k_r = \frac{D_1}{D_2} \tag{3}$$

Here, D_1 represents the hub inlet diameter, D_2 represents the diameter of the middle segment. The specific relationship is shown in Fig. 8.

Simultaneously, to more effectively characterize the variations in the external features of the multiphase pump, the ψ is introduced for the head coefficient. The head coefficient ψ is expressed as follows:

$$\psi = \frac{2gh}{{u_2}^2} \tag{4}$$

where g is the local acceleration owing to gravity, m/s^2, u_2 is the impeller outlet circumference velocity (m/s). The BBD method was employed to design three crucial factors: k_{d1}, k_{d2} and γ. Owing to the significant horizontal variations in the interval, the generated sample points were refined using the central interpolation method. This refinement aims to achieve a polynomial function response surface with reduced error, thereby enhancing the function's accuracy. Numerical simulations were conducted for each design scheme, and the ψ and η at IGVF = 50% were obtained, as presented in Table 2.

4.2 Fitting of Regression Equation

The ψ and η of each sample model under IGVF = 50% were calculated through numerical simulation. Contour diagram depicting the ψ and η with respect to each factor was generated, as illustrated in the Figs. 9 and 10.

The main factor affecting the head coefficient ψ is the air mass blockage in the middle and back section of the impeller runner. Changing the diameter of the hub inlet affects the flow rate at a certain flow rate; however, it cannot effectively inhibit air mass generation in the middle and back sections. As shown in Fig. 9, the head coefficient ψ is less affected by k_{d1}. The influence of blade inclination γ on the head coefficient ψ mainly depends on the extra centripetal force generated by the inward blade to resist the interphase crowding force, and its influence on the head coefficient ψ is stronger than that of k_{d1}. The change in the diameter of the middle section of the hub causes a non-uniform change in the flow channel area, resulting in additional acceleration that pushes the air mass in the middle and back sections

Table 2 Performance parameters of each sample model when IGVF = 50%

Model	Hub inlet coefficient (k_{d1})	Hub middle coefficient (k_{d2})	Blade inclination angle (γ)/°	Head coefficient (ψ)	Efficiency (η)/%
1	0.67	0.79	8	0.4653	61.37
2	0.75	0.79	8	0.4841	63.33
3	0.71	0.79	1	0.4740	62.43
4	0.75	0.81	1	0.4289	62.25
5	0.71	0.76	-6	0.4863	61.08
6	0.67	0.81	1	0.4585	61.24
7	0.67	0.76	1	0.4888	60.57
8	0.71	0.79	1	0.4679	62.33
9	0.71	0.76	8	0.5109	61.16
10	0.71	0.81	8	0.4398	62.65
11	0.71	0.79	1	0.4677	62.56
12	0.71	0.79	1	0.4677	62.56
13	0.75	0.79	-6	0.4726	63.31
14	0.67	0.79	-6	0.4882	60.74
15	0.71	0.81	-6	0.4469	61.71
16	0.71	0.79	1	0.4608	62.58
17	0.75	0.76	1	0.5315	62.13
18	0.77	0.83	-6	0.3987	62.69
19	0.77	0.76	6.95	0.5388	63.50
20	0.67	0.81	1	0.4153	61.39
21	0.77	0.79	2.19	0.4815	64.13
22	0.77	0.83	8	0.4259	62.92

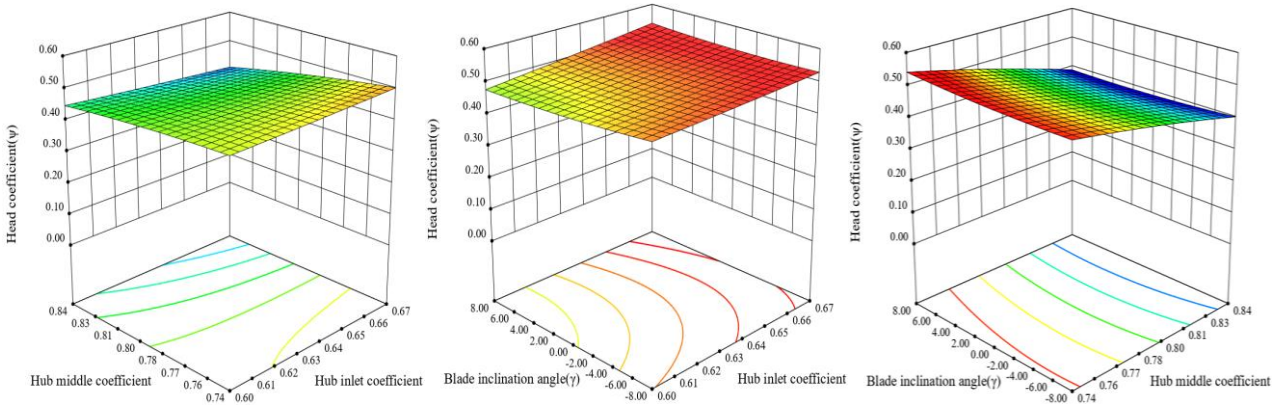

(a) γ = 0° (b) k_{d2} = 0.795 (c) k_{d1} = 0.72

Fig. 9 Head coefficient contour cloud map

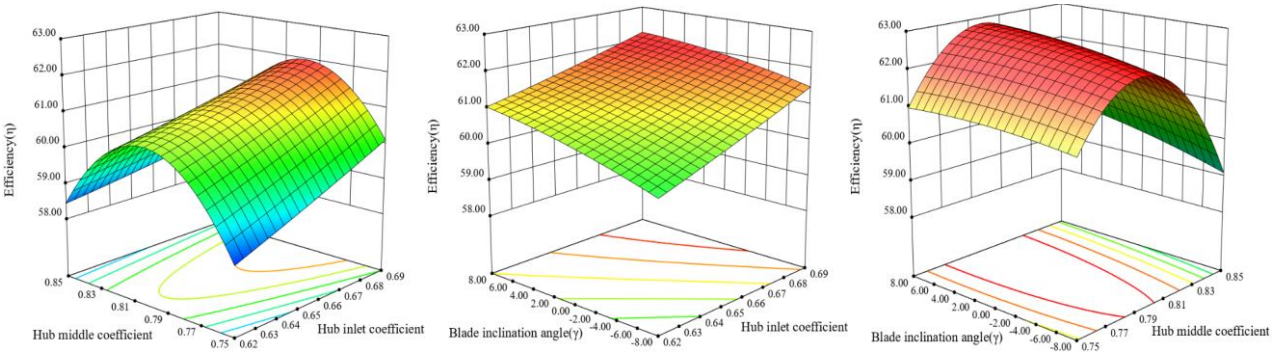

(a) γ = 0° (b) k_{d2} = 0.795 (c) k_{d1} = 0.72

Fig. 10 Efficient contour cloud map

to move to the trailing edge of the cascade. The influence of k_{d2} on the head coefficient ψ is the most obvious.

A high head coefficient should consider a small k_{d2} and a large k_{d1}, that is, the value of *k*r is large. This trend makes it easy for the flow channel area change law to make the middle and rear section velocity change laws a variable acceleration process, resulting in additional acceleration of the air mass, pushing it to move to the trailing edge, and delaying air mass accumulation.

The relationship between the efficiency and each parameter is evidently different from that of the head coefficient. As illustrated in Fig. 10, efficiency and k_{d2} exhibit a parabolic trend, with k_{d2} falling within the high-efficiency zone in the range of 0.77-0.81. The inclination angle γ and the inlet coefficient k_{d1} contributes similarly to the enhancement of efficiency.

Through a comprehensive analysis of the head coefficient ψ and efficiency η, it is observed that both parameters improve when the blade inclination angle γ is generally greater than 2°. To determine the hub structure parameters, the relative sizes of the hub inlet coefficient k_{d1} and hub middle section coefficient k_{d2} were measured using the diameter ratio *k*r. Achieving a high head coefficient requires a larger *k*r value, but this may result in low η. Conversely, a smaller *k*r value leads to higher η but lower ψ. Therefore, based on the analysis of the lift coefficient and efficiency, a *k*r value within the range of 0.94-1.02 is suggested, as it can satisfy the requirements for both high head coefficient and efficiency.

To precisely determine the optimal parameter values, mathematical relationships for the head coefficient and efficiency in terms of the dimensionless coefficients k_{d1} for hub inlet diameter, k_{d2} for hub middle section diameter, and blade inclination angle γ were derived through fitting relevant results.

$$\psi = 0.1850 + 0.9441\,k_{d1} + 0.8839\,k_{d2} - 0.0072\,\gamma - 1.94\,k_{d1}\cdot k_{d2} + 0.1633\,k_{d1}\cdot\gamma - 0.1065\,k_{d2}\cdot\gamma + 0.2455\,k_{d1}^2 - 0.5926\,k_{d2}^2 + 0.0106\gamma^2 \quad (5)$$

$$\eta = -28.53 + 27.94\,k_{d1} + 281.21\,k_{d2} - 0.3989\,\gamma - 37.70\,k_{d1}\cdot k_{d2} - 2.06\,k_{d1}\cdot\gamma + 2.80\,k_{d2}\cdot\gamma + 7.32\,k_{d1}^2 - 225.85\,k_{d2}^2 - 0.1901\gamma^2 \quad (6)$$

4.3 Significance Analysis

Using the variance (ANOVA) function analysis in Design-Expert software, R^2, *Adj* R^2, and *Pred* R^2 were employed to assess the aforementioned approximate models.

Table 3 Significance Level Analysis Results

Objective function	R^2	*Adj* R^2	*Pred* R^2
Head coefficient	0.9222	0.8911	0.8064
Efficiency	0.9306	0.8785	0.6934

$$R^2 = 1 - \frac{SS_{\text{res}}}{SS_{\text{tot}}} = 1 - \frac{\Sigma(y_i - f_i)^2}{\Sigma(y_i - \overline{y})^2} \quad (7)$$

In Eq. (7), SS_{res} is the sum of the squares of the residuals, SS_{tot} is the total sum of squares, y_i represents the value contained in the dataset, $\overline{y}$ represents the average value of the data set, f_i represents the predicted value of the response surface, R^2 indicates the degree to which the response surface fits the experimental data. As R^2 approaches 1, the degree of fit increases. As shown in Table 3, the R^2 values for the ψ and η in this model are 0.9222 and 0.9306, respectively. However, in Eq. (7), R^2 is influenced by the number of variables, meaning that R^2 tends to increase as the number of variables increases. Therefore, relying solely on R^2 is insufficient. Even if R^2 approaches 1, it cannot fully demonstrate the accuracy of the regression equation in describing the actual optimization objective and the parameter relationship. It is also crucial to analyze *Adj* R^2, which exhibits a decreasing trend opposite to R^2 when a variable is added.

$$Adj.R^2 = 1 - \frac{n-1}{n-m-1}(1 - R^2) \quad (8)$$

In Eq. (8), *n* is the sample size and *m* is the number of optimized variables. In Table 3, the head coefficients *Adj* R^2 and *Pred* R^2 were 0.8911 and 0.8064, respectively. The efficiency of *Adj* R^2 and *Pred* R^2 are 0.8785 and 0.6934, respectively. The difference between *Adj* R^2 and *Pred* R^2 for the head coefficient and efficiency was less than 0.2. Therefore, the regression equations for the head coefficient and efficiency can be considered accurate in predicting these parameters. Optimized modularization in the Design-Expert software was employed to analyze the optimal parameters of the impeller hub and blade tilt angle. The ultimate goal of this optimization was to obtain the maximum efficiency of the impeller structure parameters with a head coefficient greater than 0.53, and to provide a more accurate design parameter range and design reference for the subsequent impeller design. Consequently, the efficiency optimization condition is set to "maximization," the head coefficient is set to "greater than 0.53," and the other parameters are ensured within the specified interval range. The optimized model is modeled and analyzed by numerical calculation. The simulation and prediction results are presented in Table 4.

Table 4 Optimize impeller parameters and performance parameters

Name	Inlet coefficient (k_{d1})	Middle coefficient (k_{d2})	Blade inclination angle (γ)/ °	Predicted Head coefficient (ψ)
	0.77	0.76	6.95	0.541
Simulated Head coefficient (ψ)	Error	Predicted efficiency (η)/%	Simulation efficiency (η)/%	Error/%
0.538	0.003	63.892	63.496	0.369

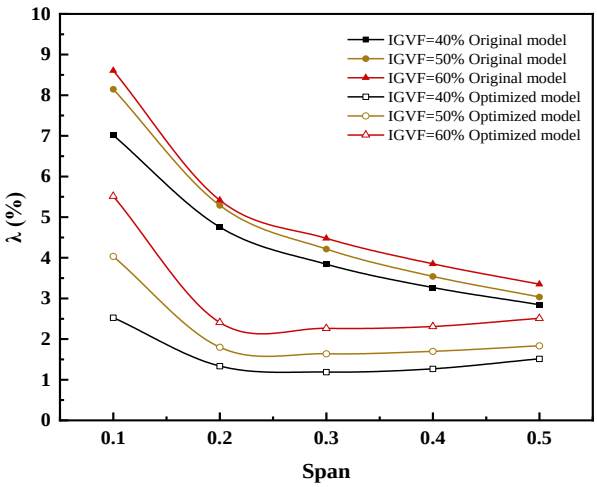

Fig. 11 Gas phase aggregation degree of the model before and after optimization

5. MODEL COMPARISON BEFORE AND AFTER OPTIMIZATION

5.1 Gas Phase Distribution of Impeller and Guide Vane

The gas phase tends to accumulate at the impeller outlet near the hub. To more precisely depict the agglomeration of the gaseous medium in the flow channel, the fluid domain of the impeller from 0.1 Span to 0.5 Span is selected as the analysis domain. The mesh area and gas content in the analysis domain are extracted, and the degree of gas accumulation, denoted by the meteorological agglomeration degree λ, is used to characterize the gas content. λ is expressed as follows:

$$\lambda = \frac{S_{GVF\geq 0.8}}{S} \times 100\% \quad (9)$$

Where S represents the grid area of the impeller analysis domain, and $S_{GVF\geq 0.8}$ indicates the area of the grid where the gas content in the analysis domain is not less than 0.8. The gas-phase aggregation degree of each Span under each IGVF of the model before and after optimization is illustrated in Fig. 11.

From the gas phase of the flow parts before and after optimization is shown in Fig. 12, for an IGVF of 40%, it can be observed that during the process of the impeller performing work on the fluid, owing to the different densities of the gas and water, the water with greater density in the mixed phase is subjected to greater centrifugal force and moves to the shroud of the impeller. The gas is driven away by the liquid phase and approaches the hub. Under the action of the inverse pressure gradient, the gas phase eventually accumulates near the blade suction surface, as shown in Fig. 12 (a). At 0.1 Span, the gas phase aggregation degree λ = 0.071, causing the flow channel to be occupied and blocked by the gas phase. This reduces the flow area and compels the fluid to alter its original flow direction to bypass the air mass. At locations away from the hub, λ decreases, with λ being 0.048 at 0.2 Span and 0.028 at 0.5 Span, indicating that the fluid is transported more as a gas-liquid mixed medium.

The optimization model involved changes in the hub diameter ratio and blade inclination angle. During the impeller operation, the hub diameter ratio modifies the flow area. Following the principles of hydrodynamics, this alteration induces an additional acceleration of the air mass during the flow process, pushing the air mass toward the trailing edge of the cascade. In addition, the inclined blade can supply an extra centripetal force to the fluid, partially offsetting the crowding force between the phases. This reduction in crowding contributes to a decreased degree of gas-liquid phase separation, ultimately diminishing the radial velocity component of the gas phase. Under the combined influence of these modifications, the gas phase accumulation speed and degree at the wheel hub side decrease. At 0.1 Span, λ = 0.025 decreases by 0.046 compared to before optimization, and λ for other spans also experiences significant decreases. The gas-phase agglomeration degree of the impeller was markedly improved, leading to enhanced pumping performance and stability, as listed in Table 5. Compared with the original model, the performance of the optimized model has been improved.

Table 5 Comparison of model performance before and after optimization

IGVF/%		40	50	60
Original model	ψ	0.502	0.495	0.485
	η/%	61.010	60.974	60.940
Optimized model	ψ	0.539	0.538	0.535
	η/%	63.547	63.496	63.271

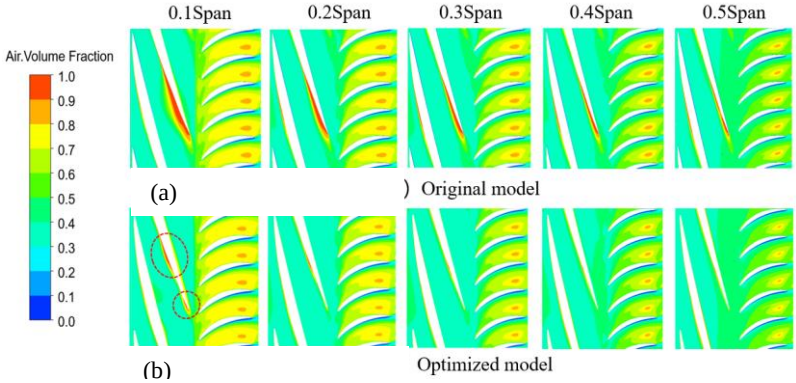

Fig. 12 Model gas phase volume fraction before and after optimization when IGVF = 40%

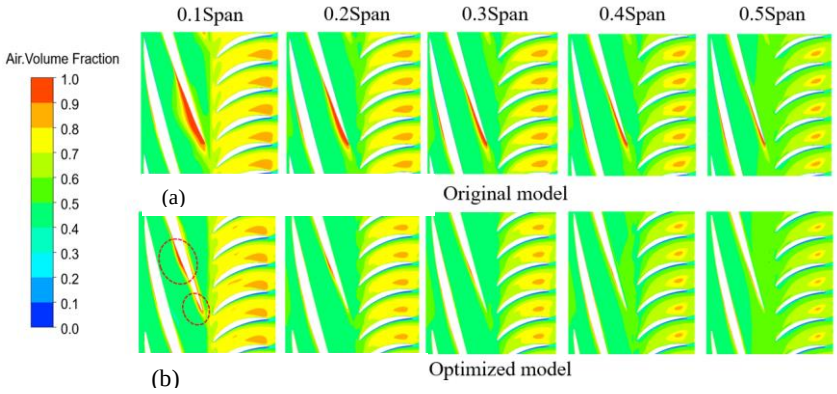

Fig. 13 Model gas phase volume fraction before and after optimization when IGVF=50%

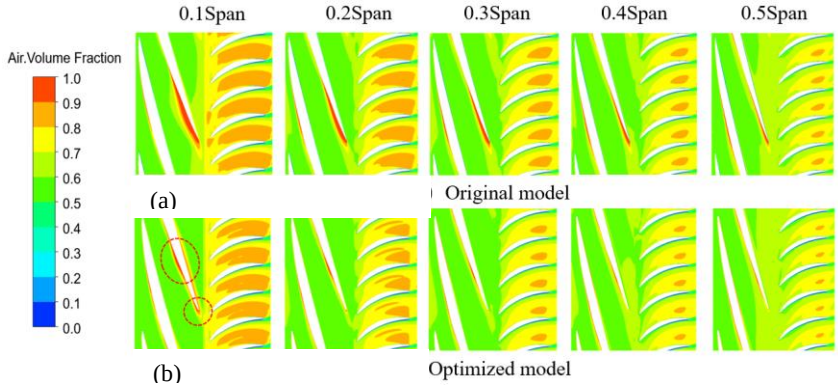

Fig. 14 Model gas phase volume fraction before and after optimization when IGVF = 60%

The comparison from Fig. 11 reveals a gradual increase in λ at each Span as IGVF increases. Comparing Fig. 12, 13 and 14, it can be seen that the area of high gas phase content in the impeller is significantly expanded, and the degree of gas phase agglomeration is gradually increased. As shown in Fig. 13 (b), after optimization, the suction surface of the inclined blade becomes more inclined along the radial direction, forcing the suction surface of the blade to generate centripetal force between the gas-liquid phase and slow down the degree of gas phase agglomeration. In comparison with the original model, λ is reduced by 0.041, reaching 0.040 at 0.1 Span, indicating a substantial improvement in gas phase agglomeration. Only a slight gas-phase agglomeration occurred at approximately 60% along the flow line.

Figure 14, it can be observed that the gas phase distribution of the impeller under the IGVF is similar to that of the 40% and 50% impellers. Before optimization, λ = 0.086 at 0.1 Span, and after optimization, it decreases to 0.055, marking a reduction of 0.031. Following the optimization, the area of high gas content in the guide vane decreased noticeably, indicating that the fluid medium from the impeller to the guide vane was more of a mixed phase. In other words, the optimization of the impeller enhanced the stability of the flow field, and the external features improved, as indicated in Table 5.

5.2 Analysis of Impeller Pressurization Ability

In order to study the effects of hub diameter ratio and blade inclination on impeller performance, the pressure changes before and after optimization were examined from two perspectives: the axial direction and the radial direction.

Figure 15 illustrates a comparison of axial section pressure of the impeller before and after optimization. The optimization model adjusts the conversion efficiency of the kinetic and pressure energies in the impeller runner by changing the hub diameter ratio. As shown in Fig. 15(b), (d), and (f), the range of the high-pressure zone in each section of the impeller expanded after optimization, which is attributed to the improved flow field stability. The pressurization capacity increased in all the axial sections.

The contribution of the tilted blade to the pressurization capacity is reflected in the change in the circumferential pressure gradient in the axial section. The optimized model is at z/H = 0.42 and 0.56, the axial force is enhanced owing to the action of the tilted blade. This enhancement not only generates a radial centripetal force, but also reinforces the circumferential pressure gradient, consistent with steering. Gas-liquid separation and gas-phase aggregation typically occurred in the middle and rear sections. Increasing the circumferential pressure gradient can interfere with the initial gas mass aggregation speed and aggregation degree, thereby delaying gas-phase aggregation.

Figure 16 shows the blade load distribution for each IGVF at 0.1 Span. It was observed that the tilted blade optimized the load distribution on the suction surface by improving the gas-phase agglomeration on the hub side

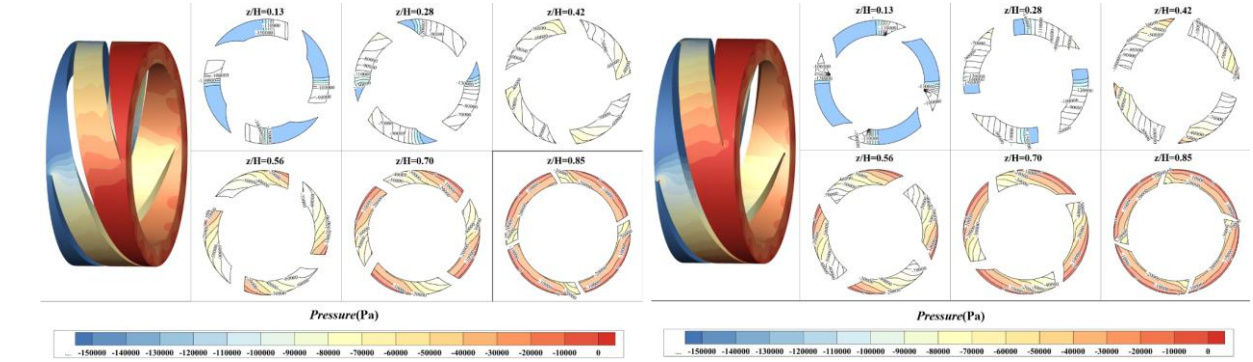

(a) IGVF = 40% original model (b) IGVF = 40% optimized model

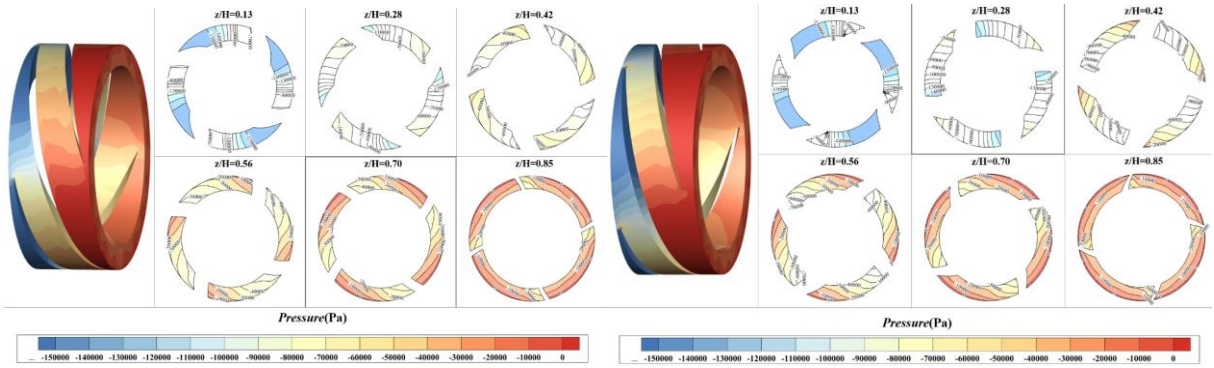

(c) IGVF = 50% original model (d) IGVF = 50% optimized model

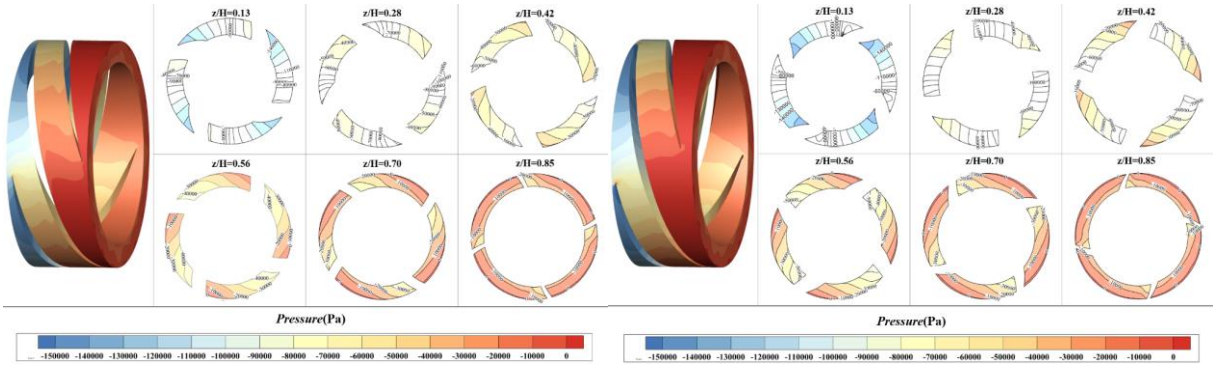

(e) IGVF = 60% original model (f) IGVF = 60% optimized model

Fig. 15 Pressure cloud image of the lower blade wheel section of IGVF before and after optimization

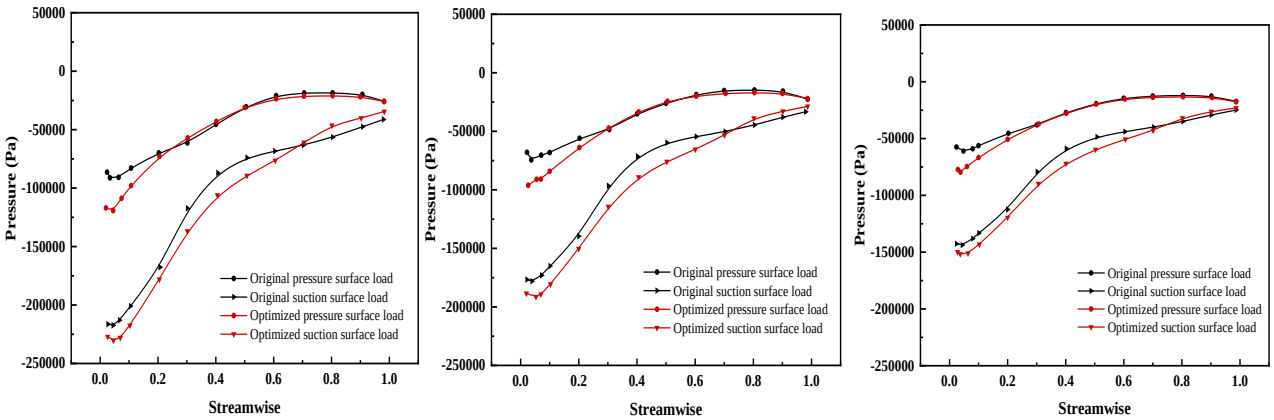

(a) IGVF = 40% (b) IGVF = 50% (c) IGVF = 60%

Fig. 16 Blade load distribution at 0.1Span under each IGVF before and after optimization

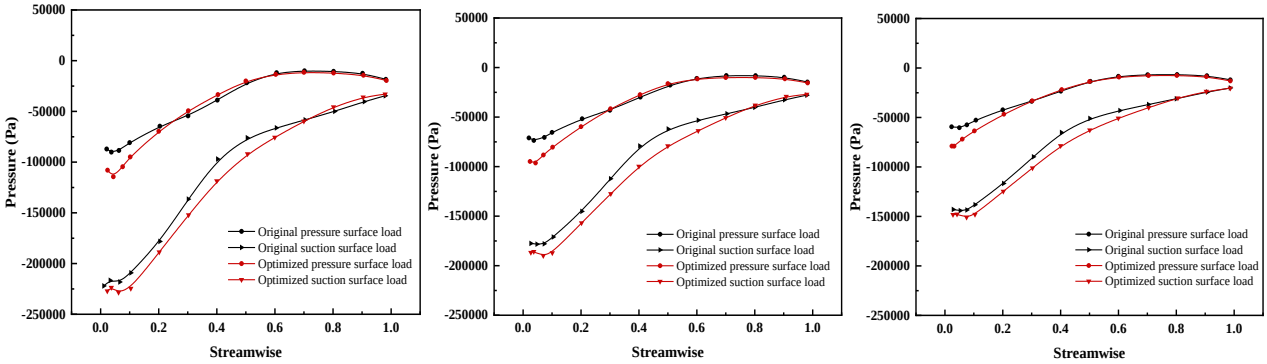

(a) IGVF = 40% (b) IGVF = 50% (c) IGVF = 60%

Fig. 17 Blade load distribution at 0.5Span under each IGVF before and after optimization

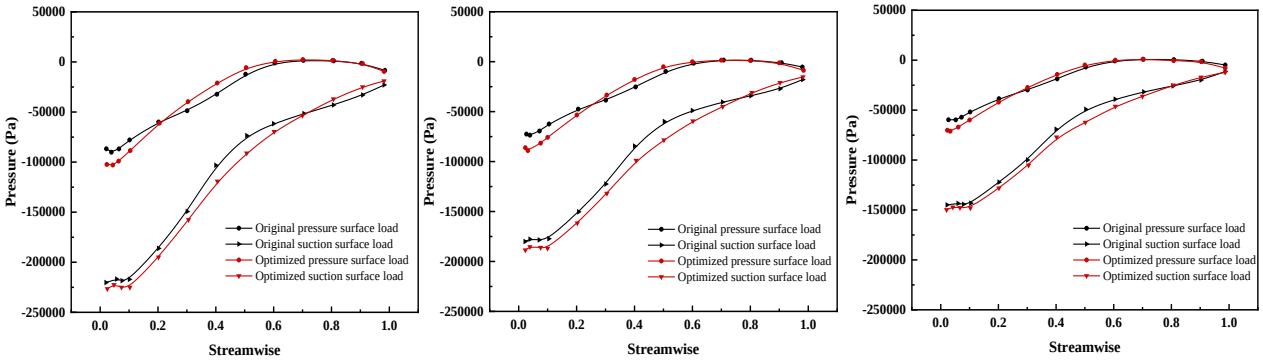

(a) IGVF = 40% (b) IGVF = 50% (c) IGVF = 60%

Fig. 18 Blade load distribution at 0.9Span under each IGVF before and after optimization

of the suction surface. Simultaneously, it maintains the load distribution on the pressure surface, contributing to functional conversion and ensuring that the head is unaffected. In the original model, the gas phase gathers on the hub side of the suction surface, resulting in the "hump" phenomenon of the load on the suction surface at 0.2 streamwise - 0.7 streamwise. The optimized impeller flow path exhibits improved gas phase agglomeration, alleviating the "hump" phenomenon caused by gas blockage. In addition, the rate of change of the load on the suction surface along the flow line was reduced.

Figure 17 illustrates the blade load distribution for each IGVF at 0.5 Span. The load variation pattern for each IGVF was similar to that at 0.1 Span. Simultaneously, the load-crossing point of the suction surface before and after optimization appears near 0.75 Streamwise. When the flow medium in the optimized impeller channel is more gas-liquid mixed phase, the flow near the suction surface becomes more stable, resulting in a significant load reduction. When the Streamwise value was greater than 0.75 Streamwise, owing to the increasing degree of inclination of the trailing edge, the optimized trailing edge of the suction surface exerted stronger constraints on the fluid, leading to an increase in the suction surface pressure.

Figure 18 shows the blade load distribution for each IGVF at 0.9 Span. Gas-phase agglomeration is also influenced by the reverse pressure gradient. After optimization, the work capacity of the model is improved, the pressure difference between the high pressure side and the low pressure side near the blade outlet is reduced, and the inverse pressure gradient in the axial direction is reduced, which is conducive to the gas phase flowing out of the impeller.

5.3 Analysis of Turbulent Kinetic Energy of Impeller and Guide Vane

Owing to the interaction between the blade and mixed medium, density differences between the light and heavy phases, and variations in the IGVF, the turbulent kinetic energy undergoes significant changes. The impeller at 0.1 Span-0.5 Span was selected as the analysis domain, and the mesh area and turbulent kinetic energy values in the analysis domain were extracted to accurately reflect the energy consumption in the flow channel. The energy dissipation degree σ is employed to characterize the energy dissipation, and its expression is as follows:

$$\sigma = \frac{S_{k\geq 10}}{S} \times 100\% \tag{10}$$

where S represents the grid area of the impeller analysis domain, and $S_{k\geq 10}$ indicates the area of the regional grid with turbulent kinetic energy not less than 10 in the analysis domain. The physical meaning of energy dissipation is that part of the energy in a system cannot be converted into useful work but exists in other forms of the system—the higher the value, the more energy is

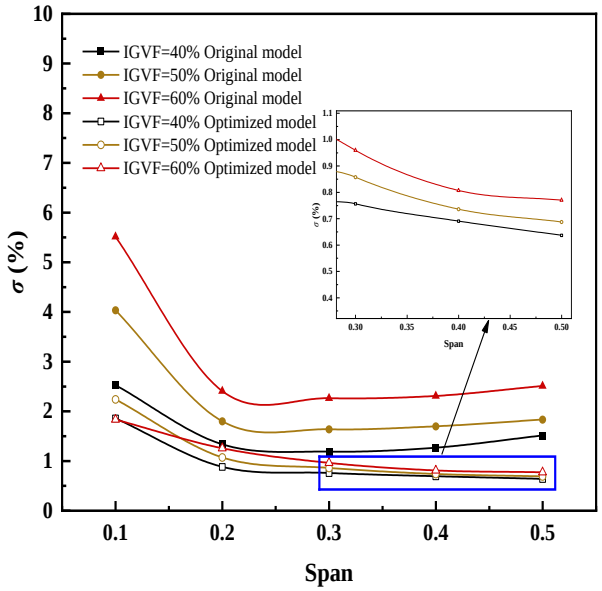

Fig. 19 Energy dissipation degree of the model before and after optimization

consumed. Fig. 19 illustrates the degree of energy dissipation of each Span under each IGVF of the model before and after optimization.

Part of the energy in the system cannot be converted into useful work but exists in other forms within the system. σ is a measure of this part of the energy consumption index. As depicted in Fig. 20, when IGVF = 40%, owing to the agglomeration of the gas phase medium, the turbulent kinetic energy of the impeller at 0.1 Span before optimization is larger, and σ is 0.072. The energy possessed by the agglomerated gas phase cannot be converted into useful work, but is dissipated in the form of heat or other forms, which also affects the conveying performance of the pump. The regions of high turbulent kinetic energy and gas phase agglomeration coincide. In Fig. 20 (a), in the region of high turbulent kinetic energy at 0.1 Span starts at approximately 40% along the streamline direction and ends at the trailing edge of the cascade. As Span increases, as shown in Fig. 19, energy dissipation σ gradually decreases until it reaches 0.5 Span, where σ is 0.026, a change that is basically consistent with the gas phase distribution.

As shown in Fig. 20 (b), the region of high turbulent kinetic energy in the optimized model shrinks. The change in the hub diameter ratio made the flow area less nonuniform. From the analysis of the continuity equation, it can be observed that the fluid generates extra acceleration to push the air mass owing to the non-uniform change in the flow area. The inclined blade reduces the radial velocity component of the gas phase and makes the gas-liquid mixing more uniform. Under the combined action of the two, σ = 0.019 at 0.1 Span of the optimized model is reduced by 0.053 compared with the model before optimization, and σ at other spans is weakened. The energy in the flow channel is more efficiently converted to useful work, and the energy dissipated in heat or other forms is reduced, thereby suppressing energy loss. decreases to 0.006 at 0.5 Span.

As shown in Fig. 19, under the influence of IGVF rise, σ gradually increases at each Span. Comparing Figures 20, 21, and 22, it is observed that the region with high turbulent kinetic energy also gradually expands. As seen in Fig. 21 (b), a small area of high turbulent kinetic energy appears along 50% of the flow line at 0.1Span in the optimized impeller flow channel, where σ is reduced by 0.056 to only 0.022. The optimized model can improve the energy conversion, efficiency and water head coefficient.

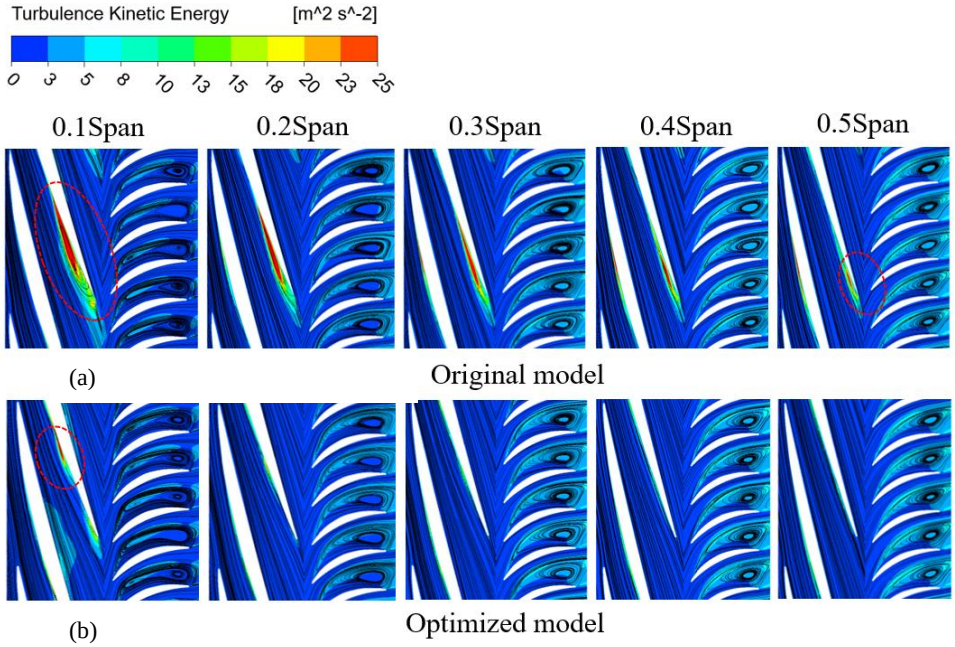

Fig. 20 Turbulent Kinetic Energy of the model before and after IGVF = 40% optimization

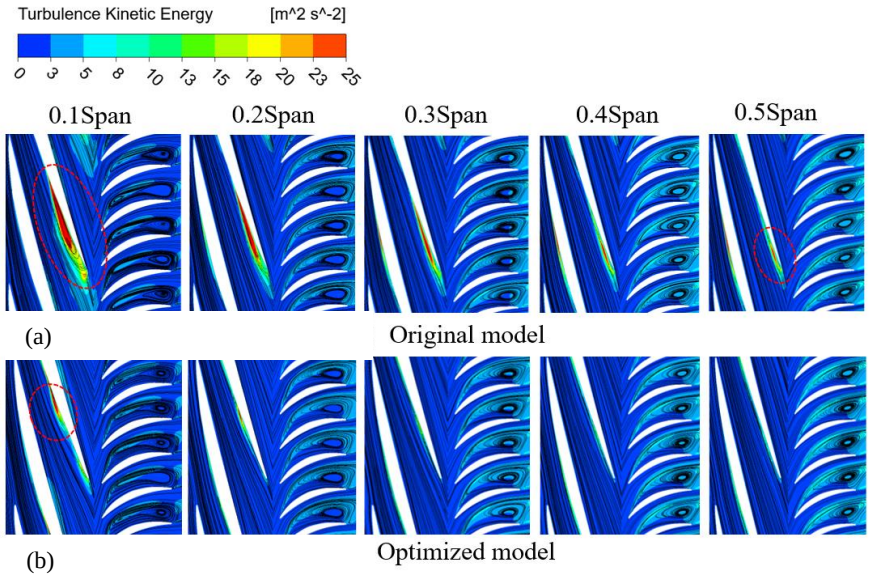

Fig. 21 Turbulent Kinetic Energy of the model before and after IGVF = 50% optimization

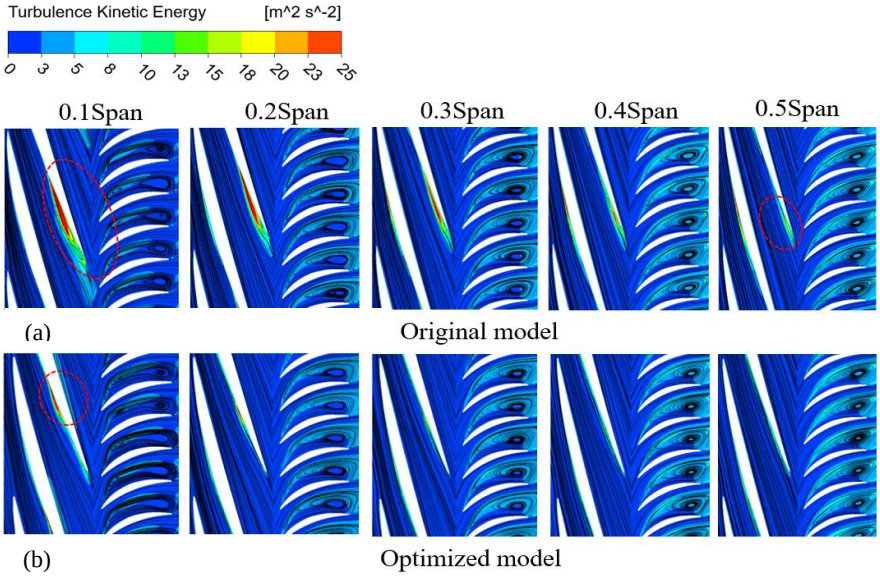

Fig. 22 Turbulent Kinetic Energy of the model before and after IGVF = 60% optimization

As depicted in Fig. 22, when IGVF = 60%, the regional distribution of high turbulent kinetic energy in the optimized impeller at the 0.1 Span is similar to that at the 40% and 50% spans. The σ = 0.018 at 0.1 Span of the impeller is optimized, which is equal to the σ value at 0.5 Span of the original model. indicating the optimization of the impeller improves the distribution of turbulent kinetic energy and enhances the functional transformation in the impeller.

6. CONCLUSION

In the process of exploring the hub parameters and blade inclination of the spiral axial flow gas-liquid multiphase pump, it was observed that a single parameter had no significant effect on the performance and may even have an inhibiting effect. However, under the coupled effects of multiple parameters, the head coefficient and efficiency exhibit more pronounced improvements. The conclusions are as follows.

1). The change in the blade inclination angle generates additional centripetal force, inhibiting the crowding of heavy and light phases and reducing the radial velocity and degree of gas-liquid separation. The optimized model adjusts the rate of change of the flow channel area by changing the hub diameter ratio, induces the air mass to generate variable acceleration, and pushes it towards the cascade trailing edge to reduce flow channel blockage.

2). To achieve a high head coefficient and efficiency, it is advisable to choose a blade inclination angle γ greater than 2°. To determine the hub structure parameters, it is essential to employ the hub diameter ratio kr to assess the relative sizes of the hub inlet coefficient k_{d1} and hub middle-section coefficient k_{d2}.

The recommended range for the *k*r value is between 0.94 and 1.02, as it satisfies the criteria for achieving an enhanced head coefficient and efficiency.

3). The optimized model improved the load distribution on the suction side, alleviating the load "hump" phenomenon caused by "gas blockage," and leading to a more stable load variation on the suction surface. The gas-phase agglomeration degree of the optimized model is significantly reduced at each span, with the largest reduction occurring at 0.1 Span. The reductions were 4.5%, 4.1%, and 3.1% when the IGVF were 40%, 50%, and 60%, respectively. Additionally, the region of high turbulent kinetic energy generated by gas-phase agglomeration in the optimized model shrinks. Energy dissipation σ significantly decreased across all spans, with the greatest reduction proportion observed at 0.1span. The decreases were 5.3%, 5.6%, and 4.3% when the IGVF was 40%, 50%, and 60%, respectively.

4). The ψ and η characteristics of the optimized model show improvement at each IGVF. Specifically, when IGVF is 40%, the ψ and η increase by 0.037 and 2.537%, respectively. At IGVF = 50%, the ψ and η increase by 0.043 and 2.522%, respectively. Similarly, at IGVF = 60%, the ψ and η increase by 0.05 and 2.331%, respectively.

ACKNOWLEDGEMENTS

This study was supported by the National Natural Science Foundation of China [Grant no. 52269022]; [Grant no. 52179086]; Central Government Guides Local Science and Technology Development Fund Projects (Grant No. 23ZYQA0320).

CONFLICT OF INTEREST

The authors declare that they do not have any conflict of interest.

AUTHORS CONTRIBUTION

W. Han supervised and guided this work. **S. Q. Yang** developed the numerical model, performed the simulation, wrote the manuscript, and prepared all the data. Finally**, R. N. Li** and **Y. P. Tian** reviewed and revised the manuscript prior to its submission. **T. Yang** proofread and wrote the manuscript.

REFERENCES

Bratu, C. (1995, October). *Two-phase pump transient behaviour*. SPE Annual Technical Conference and Exhibition (pp. SPE-30660). SPE. https://doi.org/10.2118/30660-MS

Falcimaigne, J., Brac, J., Charron, Y., Pagnier, P., & Vilagines, R. (2002). Multiphase pumping: achievements and perspectives. *Oil & Gas Science and Technology*, *57*(1), 99-107. https://doi.org/10.2516/ogst:2002007

Gié, P., Buvat, P., Bratu, C., & Durando, P. (1992, May). *Poseidon multiphase pump: field tests results.* Offshore Technology Conference (pp. OTC-7037). OTC. https://doi.org/10.4043/7037-MS

Grimstad, H. J. (2004). *Subsea Multiphase Boosting—Maturing Technology Applied for Santos Ltd's Mutineer and Exeter Field.* Paper SPE 88562 presented at the SPE Asia Pacific Oil and Gas Conference and Exhibition, Perth, Australia, 18–20 October. https://doi.org/10.2118/88562-MS

Han, W., Li, X., Su, Y., Su, M., Li, R., & Zhao, Y. (2020). Effect of thickness ratio coefficient on the mixture transportation characteristics of helical–axial multiphase pumps. *Applied Sciences*, *10*(1), 345. https://doi.org/10.3390/app10010345

Kim, J. H., Lee, H. C., Kim, J. H., Choi, Y. S., Yoon, J. Y., Yoo, I. S., & Choi, W. C. (2015). Improvement of hydrodynamic performance of a multiphase pump using design of experiment techniques. *Journal of Fluids Engineering*, *137*(8), 081301. https://doi.org/10.1115/1.4029890

Leporcher, E., Delaytermoz, A., Renault, J. F., Gerbier, A., & Burger, O. (2001, September). *Deployment of multiphase pumps on a north sea field*. SPE Annual Technical Conference and Exhibition (pp. SPE-71536). SPE. https://doi.org/10.2118/71536-MS

Li, W., Li, Z., Han, W., Li, Y., Yan, S., Zhao, Q., & Chen, F. (2023a). Measured viscosity characteristics of Fe3O4 ferrofluid in magnetic and thermal fields. *Physics of Fluids*, *35*(1). https://doi.org/10.1063/5.0131551

Li, W., Li, Z., Han, W., Li, Y., Yan, S., Zhao, Q., & Gu, Z. (2023b). Pumping-velocity variation mechanisms of a ferrofluid micropump and structural optimization for reflow inhibition. *Physics of Fluids*, *35*(5). https://doi.org/10.1063/5.0149130

Li, Z., Xu, L., Wang, D., Li, D., & Li, W. (2023c). Simulation analysis of energy characteristics of flow field in the transition process of pump condition outage of pump-turbine. *Renewable Energy*, *219*, 119480.https://doi.org/10.1016/j.renene.2023.119480

Liu, M., Cao, S., & Cao, S. (2018a). Numerical analysis for interphase forces of gas-liquid flow in a multiphase pump. *Engineering Computations*, *35*(6), 2386-2402. https://doi.org/10.1108/EC-04-2018-0161

Liu, M., Tan, L., & Cao, S. (2018b). Design method of controllable blade angle and orthogonal optimization of pressure rise for a multiphase pump. *Energies*, *11*(5), 1048. https://doi.org/10.3390/en11051048

Liu, X. D., Farhat, M., Li, Y. J., Liu, Z. Q., & Yang, W. (2023). Onset of flow separation phenomenon in a low-specific speed centrifugal pump impeller. *Journal of Fluids Engineering*, *145*(2), 021206. https://doi.org/10.1115/1.4056213

Ma, X. J, Zhang, Y, & Liu, X. R. (2020). Optimization design of impeller of multiphase pump based on

CFD method. *Journal of Xihua University（Natural Science Edition）*, *39*(1), 1–7. https://doi.org/10.12198/j.issn.1673-159X.3126

Ma, X. J., Ni, P. B., & Jia, W. B. (2015). Analysis of effect of Rotational speed on performance of spiral axial flow oil-gas mixed pump. *Gansu Science Journal*, *27*(1), 128-130. https://doi.org/10.16468/j.cnki.issn/1004-0366.2015.01.027

Mohajerani, M., Mehrvar, M., & Ein-Mozaffari, F. (2012). CFD analysis of two-phase turbulent flow in internal airlift reactors. *The Canadian Journal of Chemical Engineering*, *90*(6), 1612-1631. https://doi.org/10.1002/cjce.20674

Murakami, M., & Minemura, K. (1980). A theoretical study on air bubble motion in a centrifugal pump impeller. *Journal of Fluids Eng*ineering, *102*(4), 446-453. https://doi.org/10.1115/1.3240721

Murakami, M., & Minemura, K. (1983a). Behavior of air bubbles in an axial-flow pump impeller. *Journal of Fluids Eng*ineering, *105*(3), 277-283. https://doi.org/10.1115/1.3240986

Murakami, M., & Minemura, K. (1983b). Effects of entrained air on the performance of a horizontal axial-flow pump. *Journal of Fluids Eng*ineering, *105*(4), 382-388 https://doi.org/10.1115/1.3241015

Pei, J., Gan, X., Wang, W., Yuan, S., & Tang, Y. (2019). Multi-objective shape optimization on the inlet pipe of a vertical inline pump. *Journal of Fluids Engineering*, *141*(6), 061108. https://doi.org/10.1115/1.4043056

Saadawi, H. (2007, December*). An overview of multiphase pumping technology and its potential application for oil fields in the gulf region*. IPTC 2007: International Petroleum Technology Conference (pp. cp-147). European Association of Geoscientists & Engineers. https://doi.org/10.3997/2214-4609-pdb.147.iptc11720

Saadawi, H. (2008). Operating multiphase helicoaxial pumps in series to develop a satellite oil field in a remote desert location. *SPE Projects, Facilities & Construction*, *3*(02), 1-6. https://doi.org/10.2118/109785-PA

Shi, G. T., Li, H. L, Liu, Z. K., & Wang, S. (2019a). Effect of hub ratio on flow field characteristics in multiphase pump. *Fluid Machinery*, *48*(5),49-54. https://doi.org/10.3969/j.issn.1005-0329.2020.05.009

Shi, Y., Zhu, H., Yin, B., Xu, R., & Zhang, J. (2019b). Numerical investigation of two-phase flow characteristics in multiphase pump with split vane impellers. *Journal of Mechanical Science and Technology*, *33*, 1651-1661. https://doi.org/10.1007/s12206-019-0317-y

Stel, H., Ofuchi, E. M., Sabino, R. H., Ancajima, F. C., Bertoldi, D., Marcelino Neto, M. A., & Morales, R. E. (2019). Investigation of the motion of bubbles in a centrifugal pump impeller. *Journal of Fluids Engineering*, *141*(3), 031203. https://doi.org/10.1115/1.4041230

Suh, J. W., Choi, Y. S., Kim, J. H., Lee, K. Y., & Joo, W. G. (2017, July). *Multiphase flow analysis for air-water bubbly flow in a multiphase pump.* Fluids Engineering Division Summer Meeting (Vol. 58042, p. V01AT03A015). American Society of Mechanical Engineers. https://doi.org/10.1115/FEDSM2017-69239

Wang, C., Peng, H., Ding, J., Zhao, B. J., & Jia, F. (2013). Optimization for vortex pump based on response surface method. *Transactions of the Chinese Society for Agricultural Machinery*, *44*(5), 59-65. https://doi.org/10.6041/j.issn.1000-1298.2013.05.012

Wu, C., Zhang, W., Wu, P., Yi, J., Ye, H., Huang, B., & Wu, D. (2021). Effects of blade pressure side modification on unsteady pressure pulsation and flow structures in a centrifugal pump. *Journal of Fluids Engineering*, *143*(11), 111208. https://doi.org/10.1115/1.4051404

Zhang, J. Y., Zhu, H. W., Ding, K., & Qiang, R. (2012, November*). Study on measures to improve gas-liquid phase mixing in a multiphase pump impeller under high gas void fraction*. IOP Conference Series: Earth and Environmental Science (Vol. 15, No. 6, p. 062023). IOP Publishing. https://doi.org/10.1088/1755-1315/15/6/062023

Zhang, J., Zhu, H., Yang, C., Li, Y., & Wei, H. (2011). Multi-objective shape optimization of helico-axial multiphase pump impeller based on NSGA-II and ANN. *Energy Conversion and Management*, *52*(1), 538-546. https://doi.org/10.1016/j.enconman.2010.07.029